Research paper

Effect of electron number densities on the radio signal propagation in an inductively coupled plasma facility

Diana Luís [a,b,*], Vincent Giangaspero [c,a], Alan Viladegut [a], Andrea Lani [c], Adriano Camps [b,d,e], Olivier Chazot [a]

[a] *Aerospace and Aeronautics Department, von Karman Institute for Fluid Dynamics, Chaussee de Waterloo 72, 1640 Rhode-Saint-Genese, Belgium*
[b] *Signal Theory and Communications Department, Universitat Politecnica de Catalunya, UPC Campus Nord, C/Jordi Girona 1-3, 08034 Barcelona, Spain*
[c] *Centre for Mathematical Plasma-Astrophysics, Katholieke Universiteit Leuven, Celestijnenlaan 200B, B-3001 Leuven, Belgium*
[d] *Institut d'Estudis Espacials de Catalunya, Universitat Politecnica de Catalunya, UPC Campus Nord, C/Jordi Girona 1-3, 08034 Barcelona, Spain*
[e] *College of Engineering, UAE University, Al Ain P.O. Box 15551, Abu Dhabi, United Arab Emirates*

ARTICLE INFO

ABSTRACT

Spacecraft entering a planetary atmosphere are surrounded by a plasma layer containing high levels of ionization, due to the extreme temperatures in the shock layer. The high electron number densities cause attenuation of the electromagnetic waves emitted by the on-board antennas, leading to communication blackout for several minutes. This work presents experimental measurements of signal propagation through an ionized plasma flow. The measurements are conducted at the VKI plasma wind tunnel (Plasmatron) using conical horn antennas transmitting in the Ka-band, between 33 and 40 GHz. Testing conditions at 15, 50 and 100 mbar, and powers between 100 and 600 kW cover a broad range of the testing envelope of the Plasmatron as well as a broad range of atmospheric entry conditions. The transmitting antenna is characterized at the UPC anechoic chamber, obtaining the radiation patterns, beamwidth, and gain at the boresight direction; and an optical ray tracing technique is used to describe the electromagnetic waves propagation in the plasma flowfield inside of the Plasmatron chamber. The signal propagation measurements show clear attenuation when the signal is propagating through the plasma, varying between 2 and 15 dB depending on the testing conditions. This attenuation increases with electron number densities, which are driven by the Plasmatron power and pressure settings. Preliminary evidence of Faraday rotation effects caused by the plasma is also observed.

1. Introduction

Spacecraft entering planetary atmospheres at hypersonic velocities generate a shock wave ahead of the vehicle and consequently extreme aerodynamic heating. The high post-shock temperatures dissociate and ionize the atmospheric gases creating a plasma layer that surrounds the spacecraft. High ionization degrees affect the propagation of the electromagnetic waves emitted by the on-board communication antennas, causing attenuation, polarization rotation and refraction (i.e. trajectory bending) of the radio waves. Extreme ionization levels ultimately lead to communications blackout. Fig. 1 shows a schematic representation of this phenomenon. The radio communication blackout occurs when the electron plasma frequency of the ionized gas around the vehicle exceeds the radio frequency used for communications. The ionization degree of the gas defines the plasma frequency, f_p [Hz], which is related to the

electron number density, n_e [m^{-3}], as

$$f_p = \frac{1}{2\pi}\sqrt{\frac{q_e^2 n_e}{m_e \epsilon_0}} \approx 9\sqrt{n_e}, \tag{1}$$

where q_e and m_e are, respectively, the electron charge and mass, and ϵ_0 the free space permittivity.

Radio blackout typically lasts several minutes, depending on the trajectory and altitude of the vehicle, the properties of the atmosphere [1] and the frequency of the emitting antenna. Fig. 2 presents the flight paths, blackout intervals and corresponding link frequency bands for the Atmospheric Reentry Demonstrator (ARD), Apollo 7 and Apollo 8, and the Radio Attenuation Measurement (RAM-C II) reentry missions. The ARD [2] blackout started at an altitude of 89.8 km and ended at 40 km, lasting almost 5 min. The reentry capsule included radio frequency links with GPS constellation at 1.575 GHz, and Tracking and Data
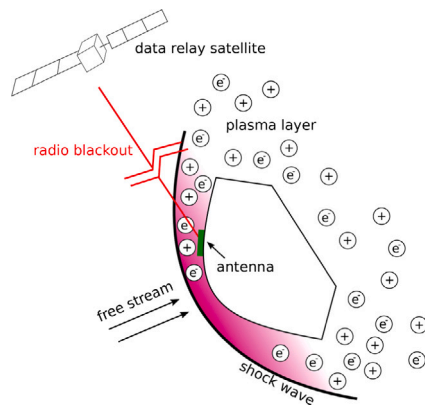
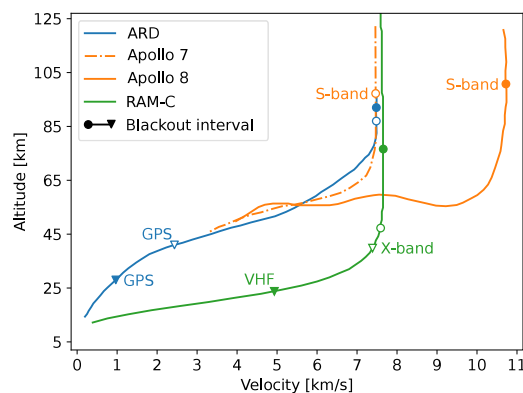Fig. 1. Schematic of the blackout phenomenon during reentry.

Fig. 2. Flight path, blackout interval, and respective link frequency band for ARD, Apollo 7, Apollo 8, and RAM-C reentry missions. (For interpretation of the references to colour in this figure legend, the reader is referred to the web version of this article.)

Relay Satellite (TDRS) at 2.267 GHz (S-band). Attenuation was more pronounced for the GPS satellite positioned forward the ARD (full blue dot in Fig. 2) than to the positioned backward (blue countered dot). No blackout of the TDRS in a backward position was experienced but plasma attenuation ranged between 86 km and 43 km, up to −25 dB. Apollo 7 and 8 [3] were equipped with S-band antennas transmitting at 2.2875 GHz. The signal losses occurred at altitudes of 97 km and 100 km, respectively for Apollo 7 and Apollo 8, and did not end before 49 km. RAM-C II [4,5] flight data was transmitted on two downlinks at frequencies of 0.2597 GHz and 9.21 GHz, corresponding respectively to VHF (full green dot) and X-band (green countered dot). Additionally, RAM-C II was equipped with fifteen reflectometer antennas from L-, S- X- and Ka-bands located along four stations along the spacecraft, and electrostatic probes. The blackout of the VHF and X-band telemetry links started at 76 km and 51 km, and ended at 23 km and 38 km, respectively. Fig. 2 motivates that the key to the reentry blackout problem lies in a reduction of the electron densities in the plasma layer or an increase of the communication frequency.

From the beginning of space exploration, different methodologies for actively reducing the plasma layer effects on radio communication attenuation and blackout have been proposed and studied. The most promising areas of research are transmission at very high frequencies, creation of a magnetic field, aerodynamic shaping effects [6], electrophilic injection [7], and Raman scattering process [8]. The first one, transmission at high radio frequencies well above the reentry plasma frequency is the simplest solution to the communication blackout problem. However, radio frequencies above 10 GHz suffer highly from atmospheric conditions [9], primarily from the signal absorption by water vapor. Of particular interest is the water vapor resonance

absorption at 22.3 GHz and the oxygen molecular absorption at 60 GHz [10]. The application of a magnetic field creates a window through which telemetry signals can pass with low attenuation, but implies flying with, at best, latest generation superconducting magnets and their associated cryogenic systems [6], potentially carrying additional weight and complexity with them. The adjustment of the vehicle leading-edge geometry is a common type of aerodynamic shaping, as it weakens the shock strength. However, sharply pointed vehicles have significant less payload capacity and suffer from more aerodynamic heating issues [11]. The injection of electrophilic materials into the ionized flow forces the recombination of free electrons with the material molecules, reducing the electron density and therefore the plasma frequency. Although this method reduces up to 30% the electron number density and up to 16% the plasma frequency [5], the reduction is not sufficient to maintain communications throughout the reentry flight. Finally, the Raman scattering process consists in placing on board of the spacecraft a source of an intense high frequency electromagnetic pump wave transmitting to the region of reflection of the signal waves from the ground. The interaction of the pump wave and the Langmuir oscillations produced in the region of the signal reflection results in the excitation of a third wave, called a Stoke wave, which travels back towards the vehicle [8]. This method has several limitations, such as collisional damping, sensitivity to plasma non-uniformities, and very short range of resonance for three-wave interactions [12].

During the 1960s, NASA's radio attenuation measurement program [13] was conducted to develop diagnostics to characterize the reentry plasma parameters and to begin in-flight testing of some mitigation methods. Those studies confirmed that the most feasible methods consisted mainly of electrophilic injection and magnetic windows opening [14]. However, no method has been successfully integrated into a spacecraft for regular flight.

Conversely to flight experiments, several experimental campaigns have been performed in ground facilities. Significant success at mitigating the blackout conditions have been observed using a Remote Antenna Assembly (RAA) in hypersonic wind tunnels for different Mach numbers [15]. A RAA is a small antenna assembly which is mounted on a pylon sticking out of the bow shock, i.e., outside the thick shock layer. These antennas generate as well a shock wave and are streamlined by plasma. Nevertheless, this study showed that acceptable ionization levels near the antennas can be achieved to allow communications. However, the RAA usually melted without the use of an active cooling system [16]. Savino et al. [17] conducted an experimental campaign in an arc jet plasma wind tunnel to reproduce the plasma frequency on ground and to numerically correlate it with the radio frequency signal loss. For that, they conducted a preliminary characterization of the plasma density and electron temperature using a Langmuir probe. This study demonstrated the capability of duplicating the ionization levels encountered during reentry, and the ability of arc jet facilities, integrated with proper numerical tools, to correctly deal with communication attenuation and blackout. When testing the performance of a heat shield protecting the antenna, Bendoukha et al. [18] explored a new method of communication called end of radio silence using an arc heated facility. A transmitter was located behind the thermal shield and the receiver equipped with a wire antenna was installed in the vacuum chamber and outside the hot gas flow to receive the radio signal during the transmissions.

Concurrently, blackout prediction and analysis try to examine the interaction between the electromagnetic waves and the ionized plasma. For that, they rely on empirical formulations and non-equilibrium hypersonic computational fluid dynamics (CFD) to estimate the electron number density in the plasma present in the propagation medium [19]. To model the electromagnetic wave propagation through the plasma, several methods can be used including the plasma frequency approach [20–22], geometrical optics or ray tracing [23], or using a finite difference scheme to solve the Maxwell equations directly [24]. The plasma frequency method is the simplest, as the other methods involve

direct simulation of the radio wave as it traverses the plasma. However, only the latter are able to accurately model the wave phenomena of reflection, refraction (ray bending), phase modulation and spectral broadening of the radio signal [25]. Ramjatan et al. [25] applied a decoupled CFD approach in combination with a simplified ray tracing algorithm to examine the reflection and refraction of the radio waves in the wake flow of the ExoMars Schiaparelli vehicle. They demonstrated that reflection and refraction can allow rays to escape the plasma sheet, which is relevant to communication brownout, and that the radio blackout was due to encapsulation of the rays by the plasma rather than absorption of the signal. Giangaspero et al. [19] further developed the ray tracing methodology by including the high frequency Eikonal approximation theory and presented the first 3D ray trajectory results for the ExoMars vehicle. The extended methodology has been also tested in Earth reentry for the ARD capsule [26]. Additionally, Giangaspero et al. [27] applied the same ray tracing technique unprecedentedly to high frequency radio signals propagating in a plasma wind tunnel, the VKI-Plasmatron facility, based on numerical simulations of the 2D axisymmetric flowfield inside the chamber. Laur et al. [28] presented a 2D ray tracing algorithm for magnetized plasmas applied to the Knapp's test case [29], which consists in an argon plasma flow impacting on a magnetohydrodynamic (MHD) probe equipped with a variable number of magnets. In the absence of a magnetic field, all the 50 rays with an initial aperture angle of 16.7° were heavily refracted towards the starting point and also reflected at the shoulder region. Applying a magnetic field using one magnet (0.25 T) led to very similar results (16.8°), while for six magnets (0.35 T) the rays were much weakly bent and the aperture angle increased to 22.2°. For a 3.5 T magnetic field an even further increase of the aperture angle (34.5°) and a very even ray distribution were detected. This led to the conclusion that a significant magnetic field strength is required, which affects first the fluid flow and second the ray propagation.

The work presented hereafter is developed in the framework of the Horizon 2020 MEESST (Magnetohydrodynamic Enhanced Entry System for Space Transportation) project [29–31], which aims at designing and testing a proof-of-concept magnetic shielding device to mitigate radio blackout and to reduce heat flux upon the surface of the spacecraft during atmospheric entry. Analytical work [32,33] showed that the magnetic field required to allow the communication frequencies to penetrate the reentry plasma and the reduction of the heat flux must be of the order of 1 T [12]. The reduction of the electron density to a value that remains below the critical one allows to restore communications during reentry [34], by opening a window in the plasma layer through which radio waves can be transmitted [35].

As part of the project, this work presents the effects of an ionized medium on the propagation of the radio signal through an air plasma flow produced with the Inductively Coupled Plasma (ICP) generator at the VKI-Plasmatron facility. A numerical section presents 3D ray tracing simulations of the signal propagating through the plasma flowfield based on ICP simulations. The experimental results include the characterization of the transmitting antenna at the UPC anechoic chamber, and the experimental characterization of the radio wave propagation and attenuation through the plasma by placing two antennas aligned perpendicularly to the plasma flow. Additionally, the results of the signal attenuation are compared to numerical electron number densities. The novelty of this work lies on the experimental coupling between radio signal and plasma flow measurements, combined with ray tracing simulations, for understanding of the signal propagation and attenuation in an ionized medium.

2. Radio communication theory

2.1. Signal propagation in ionized media

The characteristics of electromagnetic waves propagating in the atmosphere depend strongly on the operating frequency. The ionosphere has a major effect on the propagation at medium and high

frequencies (0.3–30 MHz), because radio waves in this frequency range are effectively reflected. For frequencies above 30 MHz, the waves propagate through the atmosphere with small attenuation, allowing satellite and deep space communications. At frequencies above 10 GHz, atmospheric conditions play a major role in the signal propagation, mainly due to the absorption by water vapor [10].

The ionosphere is a region of highly charged particles that form an ionized gas or plasma. As such, the ionospheric propagation theory can be extended to plasma flow on ground facilities. The "reflections" from the ionosphere are produced by the actual "refraction" as the wave propagates through this region. The refraction properties of a medium are characterized by the index of refraction $n = \sqrt{\varepsilon_r \mu_r}$, with ε_r and μ_r being the dielectric constant and the relative permeability. The index of refraction can be estimated using the Appleton–Hartree equation [36] based on Maxwell's equations and the momentum conservation of electrons as

$$n^2 = 1 - \frac{\left(\frac{f_p}{f}\right)^2}{1 - i\frac{\nu}{2\pi f} - \frac{\left(\frac{f_b}{f}\right)^2 \sin^2\theta}{2\left[1-\left(\frac{f_p}{f}\right)^2 - i\frac{\nu}{2\pi f}\right]} \pm \sqrt{\frac{\left(\frac{f_b}{f}\right)^4 \sin^4\theta}{4\left[1-\left(\frac{f_p}{f}\right)^2 - i\frac{\nu}{2\pi f}\right]^2} + \left(\frac{f_b}{f}\right)^2 \cos^2\theta}},$$

(2)

where f is the frequency of the signal, ν is the electron-heavy particle collision frequency, and θ is the angle between the magnetic field vector and the wave vector. The refractive index is dependent on the total electron number density n_e through the plasma natural frequency f_p as expressed in Eq. (1). The gyroscopic frequency of electrons induced by the presence of a magnetic field B [T] is defined as

$$f_b = \frac{1}{2\pi} \frac{q_e B}{m_e}.$$

(3)

In this formulation, the plasma is characterized by the complex refractive index n, consisting of a real part μ and an imaginary part χ as

$$n^2 = (\mu - i\chi)^2,$$

(4)

where μ represents the effect of plasma in waves propagation bending and χ is the absorptivity responsible of attenuation effects on travelling waves. The effect of collisions is expressed by the absorption coefficient κ [dB/m], that represents the exponential decrease with distance of a one-dimensional travelling wave [36], as

$$\kappa = 8.69 \times \frac{2\pi f}{c} \chi.$$

(5)

In the absence of a magnetic field ($B = 0$, $\mu_r = 1$) and neglecting collisions ($\nu \to 0$), the refractive index reduces to

$$n^2 = \varepsilon_r = 1 - \left(\frac{f_p}{f}\right)^2,$$

(6)

and the relative dielectric constant can present either negative or positive values. For positive values, the refractive index is real and the wave is refracted by the plasma according to the variation of ε_r. For negative values, the refractive index is imaginary and the incident wave is totally reflected. Additionally, for frequencies $f \gg f_p$ the relative dielectric constant is essentially one, and the wave passes through the plasma without significant refraction. Instead, if the plasma is magnetized, the waves undergo Faraday rotation by the ionized medium, and the polarization vector is rotated as the wave passes through it.

The total electron content (TEC) accumulated along a transmission path penetrating the ionosphere causes the rotation of the wave polarization (Faraday rotation), time delay and dispersion of the signal, and a change in the apparent direction of the arriving signal due to refraction. As the rotations and time delays are non-linearly dependent on the frequency, a dispersion or group velocity distortion can also occur. The magnitude of the Faraday rotation, θ_F [rad], depends on
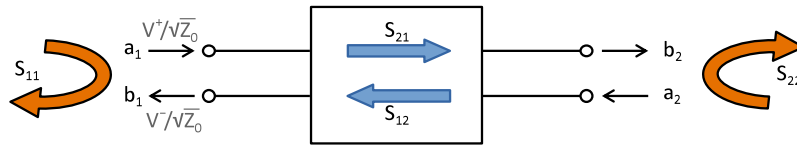
Fig. 3. Generalized two-port network.

the frequency of the radio wave, the magnetic field strength, and the electron density of the plasma as

$$\theta_F = 2.36 \times 10^4 \frac{BN_T}{f^2}, \tag{7}$$

where θ_F is the angle of rotation, B the strength of the magnetic field [T], f the frequency [Hz], and N_T the TEC [m^{-2}] expressed as

$$N_T = \int_S n_e(s)ds, \tag{8}$$

being s the propagation path [m] and n_e the electron number density [m^{-3}].

2.2. The scattering matrix: S-parameters

At high frequencies, a network is represented by its scattering matrix. This S-matrix allows to describe the properties of a multiport network by quantifying how electromagnetic energy propagates through the network. The scattering term refers to the relationship between incident and scattered (reflected and transmitted) travelling waves. The S-matrix for a N-port network contains N^2 complex coefficients (S-parameters), each one representing the magnitude and phase of a possible input–output path. The diagonal parameters are referred to as *reflection* coefficient and the off-diagonal parameters as *transmission* coefficients.

The waves going through the N-port are $\mathbf{a} = (a_1, a_2, \dots, a_N)$ and the waves travelling away are $\mathbf{b} = (b_1, b_2, \dots, b_N)$. The wave a_i going into port i is derived from the voltage wave going into a matched load. For consistency with the conversation of energy, the voltage is normalized to $\sqrt{Z_0}$, being Z_0 the characteristic impedance (often $Z_0 = 50\Omega$). The definitions of the waves a_i and b_i are

$$a_i = \frac{V^+}{\sqrt{Z_0}}, \quad b_i = \frac{V^-}{\sqrt{Z_0}} \tag{9}$$

where V^+ is the voltage of the incident wave and V^- the voltage of the reflected wave. The relation between a_i and b_i ($i \in 1, 2, \dots, N$) can be written as a system of N linear equations [37]

$$b_i = S_{ii}a_i + S_{ij}a_j, \tag{10}$$

where the j subscript stands for the port that is excited (the input port), and the i subscript for the output port. Physically, S_{ii} is the input reflection coefficient with the output of the network terminated by a matched load ($a_j = 0$); S_{ij} is the transmission from port j to port i; and S_{jj} the output reflection coefficient. The S-matrix is symmetric, which means that interchanging the input and output ports does not change the transmission properties, and therefore $S_{ij} = S_{ji}$. Fig. 3 represents a generalized two-port network with a characteristic impedance of Z_0.

2.3. Radiation pattern

A radiation pattern is a graphical representation of the radiation properties of an antenna as a function of spherical coordinates (θ, ϕ). Usually, the radiation pattern is determined in the far-field region, i.e. for $r \gg 2D^2/\lambda$, with D being the largest dimension of the antenna and λ the wavelength [38]. Various parts of the radiation pattern are referred to as lobes, which correspond to a portion of the radiation pattern bounded by regions of relatively weak radiation intensity. The main lobe contains the direction of maximum radiation. All others are

called secondary lobes, and usually represent radiation in undesired directions. The half-power beamwidth (HPBW) corresponds to the angular separation measured on the major lobe in which the magnitude of the radiation pattern decreases by 50% (or 3 dB) from its peak value.

The performance of an antenna is often described in terms of its principal E- and H-planes [38]. The E- and H-planes are defined as the planes containing, respectively, the electric field vector and the direction of maximum radiation, and the magnetic field vector and the direction of maximum radiation. Therefore, the E- and H- planes are orthogonal to each other and they both contain the propagation vector. The polarization of an antenna is defined as the orientation of the electric field vector. When the electric field in a given direction is always directed along a line, the polarization of the antenna is linear. However, real antennas generate both a co-polarization field and a cross-polarization field. The first corresponds to the polarization the antenna is intended to radiate, while the latter corresponds to the component of the electric field orthogonal to the desired polarization. The antenna polarization $\mathbf{P}$ can be described in terms of (P_θ, P_ϕ) or decomposed with respect to two orthogonal polarization unit vectors [10] as

$$\mathbf{P}(\theta, \phi) = P_\theta(\theta, \phi)\hat{\mathbf{i}}_\theta + P_\phi(\theta, \phi)\hat{\mathbf{i}}_\phi = P_{co}(\theta, \phi)\hat{\mathbf{i}}_{co} + P_{cross}(\theta, \phi)\hat{\mathbf{i}}_{cross}, \tag{11}$$

begin (P_{co}, P_{cross}) referred to as the co- and cross-polarization components, respectively. Ultimately, these can be written is terms of (P_θ, P_ϕ) [39] as

$$\begin{aligned} P_{co} &= P_\theta \cos(\alpha - \phi) + P_\phi \sin(\alpha - \phi), \\ P_{cross} &= -P_\theta \sin(\alpha - \phi) + P_\phi \cos(\alpha - \phi). \end{aligned} \tag{12}$$

where α is the co-polarization angle, normally chosen parallel to the current flow on the antenna.

3. Experimental facility and numerical tools

3.1. VKI plasmatron facility

The Plasmatron at the von Karman Institute for Fluid Dynamics (VKI) is an inductively-coupled plasma (ICP) wind tunnel [40], that creates a high enthalpy, highly dissociated subsonic gas flow for reproduction of the aerothermodynamic environment found in hypersonic flight regimes. This facility has been extensively studied by Bottin et al. [40,41]. Its basic concept consists of a quartz tube with an internal diameter of 200 mm and 5 mm thickness surrounded by a coil, which is connected to a 1.2 MW generator that provides high voltage (2 kV) and high frequency (400 kHz) current. This induces an electromagnetic (EM) field inside the tube, that forces residual charged particles in the flow to form eddy currents which heat up the gas by Joule effect. The gas injection is done through an annular inlet upstream to the coil. Due to the induced EM field, the gas ionizes and the flow exits the torch to enter into a vacuum chamber of 1.4 m in diameter as a plasma plume of 160 mm in diameter. The plasma exits the vacuum chamber through a diffuser, and it is cooled down by a water cooled heat exchanger. The vacuum system consists of a set of three pumps. After proper dilution, the recombined gases are finally released to the atmosphere through an exhaust. Complementary systems are responsible for the gas circulation, cooling, and diagnostics. An absolute pressure transducer (Memberanovac DM 12, Leybold Vacuum) measures the static pressure (p_s) in the test chamber. As the plasma jet is low subsonic (Ma ≈ 0.1),
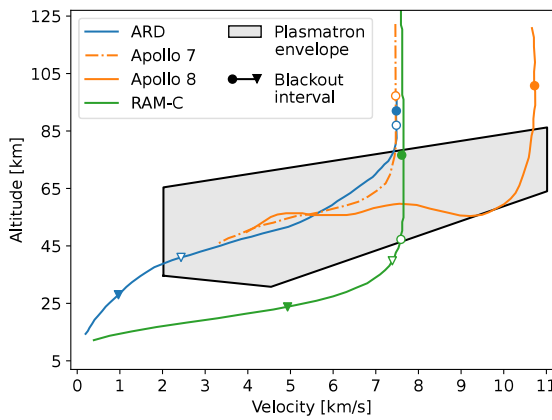
Fig. 4. Plasmatron envelope (based on the work of Panerai [44]), and flight profiles for ARD, Apollo 7, Apollo 8, and RAM-C II missions.

the static pressure is assumed constant inside the chamber. The static pressure uncertainty can be considered to be $\pm 10\%$ due to the stability of the vacuum pumps [42,43]. The gas mass flow rate ($\dot{m}_{gas}$) supplied to the torch is monitored through a calibrated gas rotameter (Bronkhorst EL-Flow F-203AV), while the Plasmatron control system records the electric power (P_{el}) supplied to the induction coil. Up to three probes can be mounted onto holders which are remotely activated to be injected and retracted from the plasma jet. Suitable quartz windows installed on the two sides of the vacuum chamber provide the necessary optical access in the direction perpendicular to the plasma flow.

Fig. 4 presents the operational envelope of the Plasmatron as a function of reentry altitudes versus velocity [44], overlapped with the flight profiles presented in Fig. 2. Most of the blackout intervals overlap with the flight duplication situations in the facility which gives favourable conditions for the study of communication blackout during Earth atmospheric reentry.

3.2. UPC anechoic chamber

The anechoic chamber at the Universitat Politècnica de Catalunya (UPC) [45] allows to remotely measure radiation diagrams from 0.8 to 40 GHz. The chamber is 10 m long, 7.5 m wide, and 6 m high, with a total volume of 450 m^3. The antenna patterns are measured in near field and transformed to far field using a software developed at UPC [46], based on the classical algorithms described by Hansen [47].

3.3. ICP magnetohydrodynamics solver

The subsonic steady state plasma flowfield in the Plasmatron chamber is numerically simulated using the in-house VKI ICP magnetohydrodynamics (MHD) solver [48,49]. This solver couples the Maxwell equations with the Navier–Stokes equations under Local Thermodynamic Equilibrium (LTE) and axisymmetric steady flow assumptions, within the Computational Object-Oriented Library for Fluid Dynamics (COOLFluiD) [50]. The resulting COOLFluiD ICP solver simulates the interaction between the electromagnetic field around the coil and the gas passing through, with the aim of reproducing the whole Plasmatron chamber. The ICP computations use the VKI-developed Mutation++ library [51] to determine thermodynamic and transport properties of the 11-species air mixture, including O_2, N_2, O_2^+, N_2^+, NO, NO^+, O, O^+, N^+, N and e^-. In the simulations, all the walls are cooled down to 350 K and the annular injection of the gas is imposed at the inlet. The input parameters are p_s, $\dot{m}$, and P_{el}, which are measured during the test as described above. To note that the exact value for the numerical power generating the plasma is unknown and generally an efficiency of 50% of the electric power is assumed.

3.4. Ray tracing solver

Numerical analysis of communication blackout involves calculating the electron number density profiles from CFD simulations and modelling the radio signal propagation through the plasma. In these simulations, any plasma variation in time is considered slower than the signal propagation allowing to consider a steady plasma flow while solving the wave propagation [27]. The BlackOut RAy Tracer (BORAT) solver is a numerically efficient ray tracing algorithm for space reentry communications, developed by the University of Luxembourg and KU Leuven. In this algorithm the electromagnetic waves are discretized as a beam of rays, which means that the rays are independent and uncoupled with respect to each other, and independent from polarization.

The application of ray tracing consists in computing the optical properties of the plasma governing the propagation of the radio waves in the ionized medium. The flowfield solutions obtained from ICP simulations contain the required information to build the optical model of the plasma, which is based on the Appleton–Hartree equation (Eq. (2)). In the context of this solver, the reduced form of the equation for unmagnetized plasmas ($B = 0, \mu_r = 0$) is used. This approach neglects magnetic fields as observed for the general case of atmospheric reentry flights. The resulting equations are a direct function of the electron number density n_e (through f_p) and of the collision frequency ν. By integrating the absorption coefficient (Eq. (5)) along the path of the transmitted signal, it is possible to calculate the total attenuation due to absorption by collision with charged particles.

The algorithm implemented in the BORAT solver belongs to the family of *shooting and bouncing* ray tracing (SBR) technique [52]. In this approach the rays are emitted from the transmitting antenna location and integrated in the numerical domain until they emerge from the plasma. The ray integration technique implemented is an advanced ray tracing method based on the Eikonal equation. The Eikonal equation, derived as an approximate solution of Maxwell's equations in the high-frequency range limit [53], can be written as

$$|\nabla S| = \mu, \tag{13}$$

where S is the normalized Eikonal phase function, defining the wavefront surface of a travelling electromagnetic wave, and μ is the real part of the refractive index of the medium. The characteristic solution of the Eikonal equation defines the rays trajectories, which ultimately are only dependent on μ and f.

To summarize, the numerical strategy for the BORAT ray tracing analysis is composed by (1) CFD simulations of ionized plasma flows, (2) computation of the optical properties of the plasma by applying the Appleton–Hartree equation, (3) application of the characteristic solution of the Eikonal equation for propagation of the electromagnetic waves through the plasma, combined with prescribed initial conditions in terms of position and angle of the emitted ray.

4. Experimental setup

4.1. Design of the communication system

Knowing the natural frequency of the plasma is critical to select the appropriate target frequencies in any blackout experiment. A preliminary numerical analysis is performed to estimate the plasma frequency and, consequently, to design the appropriate communication system for an air plasma. The subsonic steady state plasma flowfield in the Plasmatron chamber is numerically simulated using the COOLFluiD ICP solver. The following analysis considers an existing database of simulations at a constant air mass flow of 16 g/s, static pressures of 15, 50 and 100 mbar, and varied numerical powers, under LTE assumption. The three positions marked in Fig. 5 are probed along the center of the jet axis for the analysis. They correspond to 20, 30 and 40 cm from the torch exit. Fig. 6 summarizes the evolution of the numerical
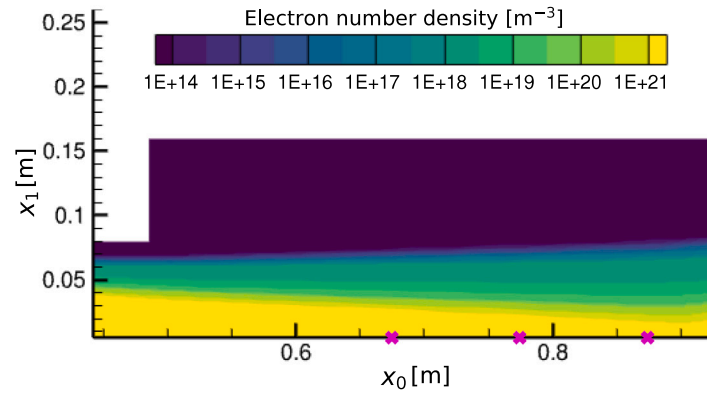
Fig. 5. Electron number density distribution of an air 11-species mixture simulated with COOLFluid ICP at 16 g/s, 15 mbar and 164 kW numerical power.
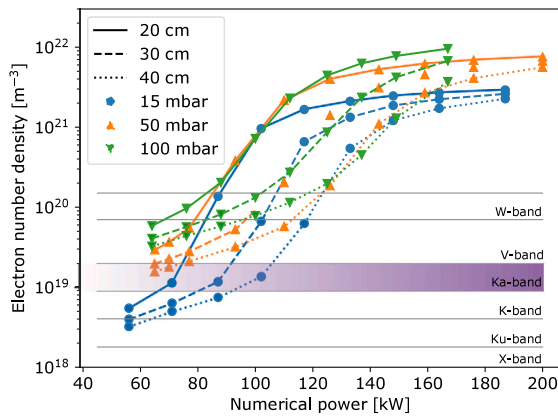

Fig. 6. Numerical evolution of the numerical electron number densities for an air mixture along the axis of the jet.

Table 1
Details about the instruments.

Instruments	Connectors	Operating frequency [GHz]	Link budget
Antenna	Custom flange	33–38.5	15 dBi
Mode transition	Custom flange	33–38.5	0 dB
Adaptor	Custom flange - 2.92 mm (f)	26.5–40	−0.4 dB
Cable	2.92 mm (m) - 2.92 mm (f)	Up to 46	−2.62 dB/m
DC block	2.92 mm (m) - 2.92 mm (f)	0.01–40	−0.75 dB
VNA	2.92 mm (m)	0.01–40	10 dBm

electron number densities with static pressure and numerical power, and communication bands between 8 GHz and 110 GHz or equivalently to electron number densities between 7.9×10^{17} m^{-3} and 1.5×10^{20} m^{-3}. Simulations show that the further away from the torch exit, the lower the electron number densities. An increase in sensitivity is observed at intermediate powers. Based on these results, the Ka-band is selected as the most appropriate for blackout experiments in the Plasmatron. Indeed, this bandwidth allows to study testing conditions where the signal can propagate through the plasma (if $f_p < f$) and conditions in complete blackout (if $f_p > f$).

4.2. Instrumentation and calibration

From the previous analysis, the communication system is defined in the Ka-band. The setup is composed of two sets, each comprising a conical horn antenna with a circular waveguide, linear polarization and 15 dBi gain (MI-wave 262A-15/0.250), a mode transition (MI-wave 284–0.250) and a waveguide to coax adapter (MI-wave 411 A). Each of these sets is connected to, respectively, a 3 m and a 3.5 m flexible microwave cable (Huber-Suhner SUCOFLEX 102), and a DC block (MI-wave 8141 A). The transmission and reception of the signal are accomplished with a vector network analyser (VNA, Rohde and Schwarz ZNB40). Some technical specifications about these parts are summarized in Table 1 and a schematic of the experimental setup is presented in Fig. 7. The combination of these instruments allows to operate between 33 and 40 GHz. The start and end sampling frequencies of the VNA can be defined in one of three modes: *sweep*, which measures through the entire available frequency range; *single*, which records only

one central frequency ($f_c \pm 1$ Hz); and *band*, which comprises a small band around the central frequency ($f_c \pm 0.1$ GHz).

Alignment and calibration of the test setup are carried out every day of testing. The alignment is done using a 360° self-levelling laser (Makita SK700D), ensuring that the centers of both antennas remain on the horizontal plane passing through the center of the torch, and on the vertical plane at a certain distance from the torch exit. The systematic calibration of the system is performed using a 2.92 mm network analyzer calibration kit (Rohde and Schwarz ZN-Z229). This type of calibration ensures that the effects of cables and DC blocks, and all systematic errors in general are canceled out before the measurements of the radio signal of the antennas. TOSM (thru-open-short-match) full 2-ports calibrations are performed, to correct all four S-parameters.

4.3. Testing conditions

To study the signal propagation in ionized media and to try to correlate them with the amount of electrons in the flow, several conditions are tested. These conditions allow gathering data in the operating envelope of the Plasmatron facility. A summary of the testing conditions is presented in Table 2. Three distinct pressures and two different distances between the antennas and exit of the torch are tested, for increasing electric powers.

For each of the targeted pressures, twenty measurements without plasma are taken. To proceed with the experiments, the Plasmatron is switched on and the air mass flow is set to 16 g/s with the calibrated rotameter. The vacuum pumps are then regulated until the target static pressure is reached inside the chamber. Once the required conditions are reached, fifty consecutive samples are taken.

4.4. Attenuation and statistical analysis

The measured parameters correspond to the S-parameters described in Section 2.2, that are complex numbers and that can be written, in linear units, as

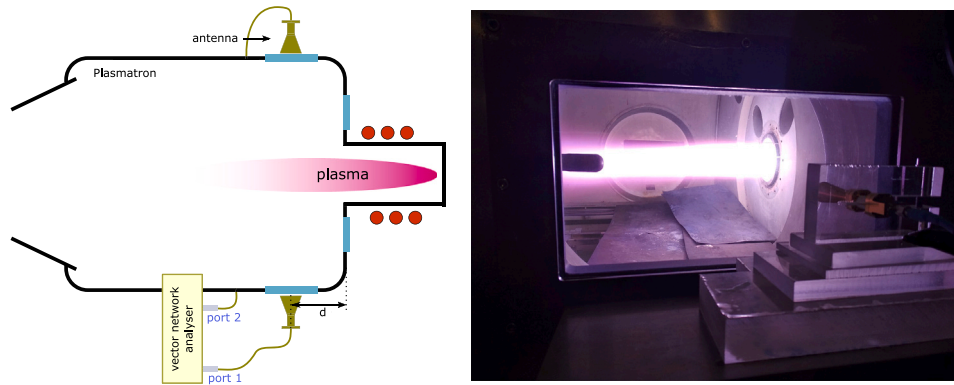$$S = |S_{[l.u.]}|e^{i\phi_S}. \tag{14}$$

Fig. 7. Schematic of the experimental setup (left) and picture taken during a test (right).

Experimentally both magnitude $|S|$ in [dB] and angle ϕ_S in [degrees] are acquired as a function of frequency. In linear units the S-parameters are proportional to the electric field $|E|$ and are computed as $|E| \propto 10^{|S_{[dB]}|/20}$. The following statistical analysis can be done either as a function of frequency, or over the total number of samples and frequency range. For each condition tested, an average $|\overline{E}|$ and standard deviation $\sigma_{|E|}$ of the signal magnitude is computed in linear units.

To study the influence of the plasma, the attenuation between the averaged signal magnitude with and without plasma is considered in this study. This method allows to neglect the influence of the quartz windows and intrinsic reflections on the metallic walls of the chamber. In linear units, the mean attenuation can be written as

$$\overline{A} = \frac{|\overline{E_{ON}}|}{|\overline{E_{OFF}}|}, \tag{15}$$

or, equivalently, in decibels [dB] as

$$\overline{A}_{[dB]} = 20 \log_{10}\left(\overline{A}\right) = \overline{S_{ON}}_{[dB]} - \overline{S_{OFF}}_{[dB]}. \tag{16}$$

The main source of uncertainty considered in this work is the random standard uncertainty ($\sigma_{\overline{E}}$), which depends on the number of samples N acquired during a certain condition. This uncertainty can be defined, for a normally distributed population and large number of samples, as

$$\sigma_{\overline{E}} = \frac{\sigma_E}{\sqrt{N}} \times 1.96, \tag{17}$$

for a 95% confidence interval. The standard deviation of the mean attenuation due to the plasma is computed according to Taylor's expansion and, ultimately, it can be written as

$$\sigma_{\overline{A}} = \sqrt{\left(\frac{1}{|\overline{E_{OFF}}|}\right)^2 \sigma_{|\overline{E_{ON}}|}^2 + \left(-\frac{|\overline{E_{ON}}|}{|\overline{E_{OFF}}|^2}\right)^2 \sigma_{|\overline{E_{OFF}}|}^2}. \tag{18}$$

being $\sigma_{|\overline{E_{OFF}}|}$ and $\sigma_{|\overline{E_{ON}}|}$ the standard deviations of the mean magnitude of the signal propagating in vacuum and in a plasma flow, respectively.

To plot the mean attenuation and respective uncertainty in decibels [dB], the following method is implemented

$$20 \log_{10}\left(\overline{A} \pm \sigma_{\overline{A}}\right), \tag{19}$$

either as function of frequency or as a total averaged values over the frequency range.

5. Ray tracing simulations

The subsonic steady state 2D axisymmetric plasma flowfield in the Plasmatron chamber is numerically simulated using the COOLFluiD ICP solver. As the domain of the simulation does not include the full chamber, the converged solution is then extrapolated to the rest of

Table 2
Summary of testing conditions.

Distance [cm]	Static pressure [mbar]	Electric power [kW]	Mode
40	15	100, 200, 320, 400	Sweep
40	50	100, 200, 320, 400, 500, 600	Sweep
40	100	200, 320	Sweep
30	15	100, 150, 200, 320, 400, 500, 600	Sweep
30	50	100, 150, 200, 320, 400, 500, 600	Sweep
30	100	150, 200, 320, 400, 500, 600	Sweep
30	15	100, 125, 150, 175, 200, 320, 400, 500, 600	Single
30	50	100, 125, 150, 175, 200, 320, 400, 500, 600	Single
30	100	125, 150, 175, 200, 320, 400, 500, 600	Single
30	15	100, 125, 150, 175, 200, 320, 400, 500, 600	Band
30	50	100, 125, 150, 175, 200, 320, 400, 500, 600	Band
30	100	125, 150, 175, 200, 320, 400, 500, 600	Band

the domain to match the chamber diameter. Finally, the solution is revolved around the symmetry axis ($x_1 = 0$) to obtain the flowfield in a simplified 3D domain of the Plasmatron chamber. The optical parameters of the flow describing the propagation of an electromagnetic wave in an ionized medium are computed based on the Appleton–Hartree equation formulated in Section 3.4. These include the refractive index μ (Eq. (4)) and the absorption coefficient κ (Eq. (5)).

Fig. 8 shows different views for the ray paths for the 15 mbar and 164 kW numerical power test case, considering the transmitting antenna positioned at 30 cm from the torch exit, a transmitting frequency of 40 GHz, an antenna beamwidth of 23°, and 1350 rays, without including reflections on the boundaries. The receiving antenna is not accounted in the numerical results but in the experimental setup is aligned to the transmitting antenna, on the opposite side of the chamber, as illustrated by the pink dot. According to these simulations, if no wall reflections occur, none of the rays reaches directly the receiving antenna due to the bending caused by the plasma. However, due to its large beamwidth (exemplified with a very simple approach by the dashed pink line), the receiving antenna still receives some signal. Fig. 9, that represents an yz view of a simulation for 15 mbar, 71 kW numerical power, shows that when decreasing power the bending angle decreases and more rays reach the measurement area of the receiving antenna. The bending is represented by the real part of the refractive index μ, that is directly related with the electron number density, which decreases with the decrease of power (as illustrated in Fig. 6). No significant differences are observed when comparing the numerical signal propagation for transmitting frequencies between 33 and 40 GHz.
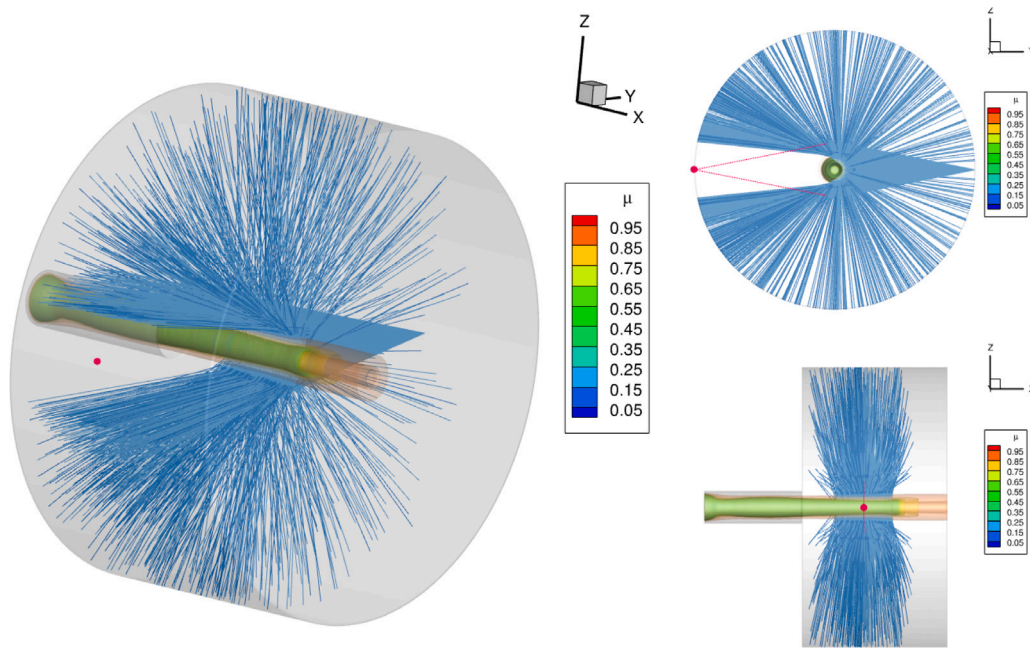
Fig. 8. Ray tracing simulations (1350 rays) for 15 mbar, 164 kW numerical power, 40 GHz with the antenna on the side window. (For interpretation of the references to colour in this figure legend, the reader is referred to the web version of this article.)
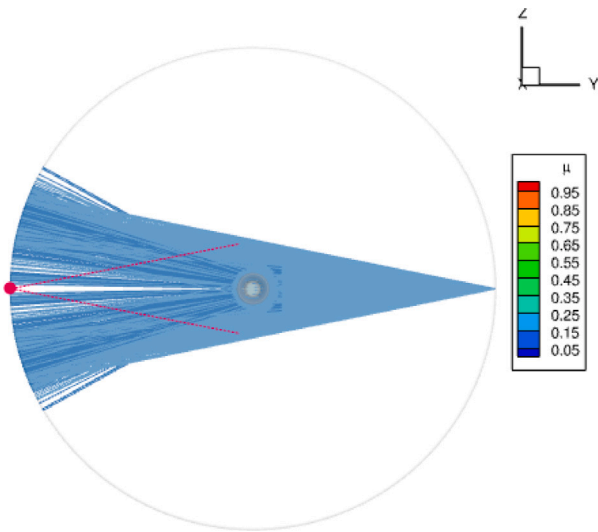

Fig. 9. View of *yz* plane of the ray tracing simulations (1350 rays) for 15 mbar, 71 kW numerical power, 40 GHz. (For interpretation of the references to colour in this figure legend, the reader is referred to the web version of this article.)

6. Experimental results

6.1. Antenna characterization

A full characterization of the antenna pattern is conducted at the UPC anechoic chamber. The reference antenna is a standard gain horn antenna (HengDa Microwave HD-320SGAH20), operating between 26.5 and 40 GHz. The measurements of the radiation pattern are taken at three specific frequencies (34, 37 and 40 GHz). The sampling step is 1°, which means 360 measurement points along ϕ direction and 181 points along the θ direction. The antenna gain measurements along the boresight direction correspond to 351 points equally distributed between 33 and 40.5 GHz. Fig. 10 illustrates the experimental setup

Table 3
3 dB beamwidth and peak cross-polar values for H- and E-planes for the measured frequencies.

Frequency [GHz]	HPBW		Peak cross-polar value	
	H-plane	E-plane	H-plane	E-plane
34	31.96°	27.77°	−27.74 dB	−27.21 dB
37	30.43°	25.55°	−25.07 dB	−25.74 dB
40	28.20°	23.67°	−22.82 dB	−22.74 dB

(left) for characterization of the antenna mounted on the anechoic chamber (right).

Based on the measured P_θ and P_ϕ field components, the antenna pattern is transformed to the co- and cross-polarization components, following Eq. (12). Fig. 11 presents these normalized components at the H-plane ($\phi = 0°$ and $\phi = 180°$) and E-plane ($\phi = 90°$ and $\phi = 270°$). Well-behaved linear polarization and broadside radiation patterns are obtained, similar in-between the different frequencies tested. Additionally, the sidelobes levels are low, below −17 dB, as well the cross-polarization levels at both planes which do not exceed the −20 dB (see Table 3). From the radiation patterns, also the HPBW is extracted and the results are summarized in Table 3.

Fig. 12 presents the evolution of the antenna gain along the boresight direction. In the operating frequencies, the antenna gain is quite constant at around 15 dBi, with slightly higher gain between 35.5 and 39.5 GHz, and decreasing performance for higher frequencies.

6.2. Influence of the metallic walls and windows without plasma

From the gains and losses in the communication system (Table 1), a theoretical received to transmitted magnitudes ratio can be estimated. The radio link budget sums the transmitted power along with the gains and losses of every subsystem to determine the signal strength arriving at the receiver input. For this case, the link budget equation for the radio communication system is written as

$$P_R - P_T = G_T - L_T - L_{FS} + G_R - L_R,\qquad(20)$$

where $P_R - P_T$ [dB] is the ratio (in linear units) of the received and transmitted powers (converted to dB) as measured by the VNA. G_T
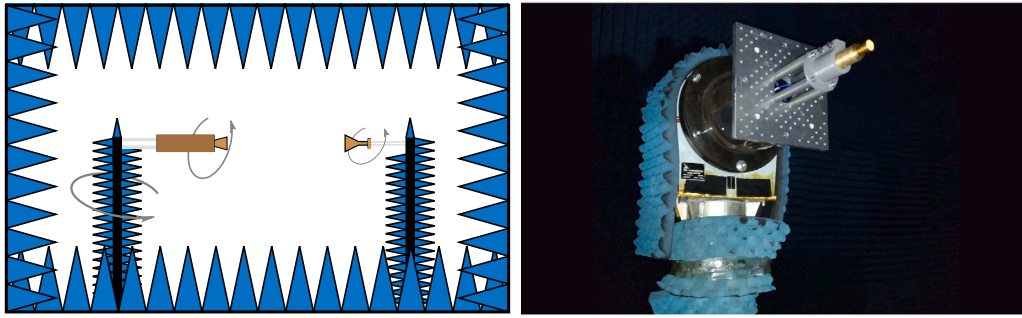
Fig. 10. Setup for antenna pattern characterization in the anechoic chamber (left), and antenna under test mounted (right).
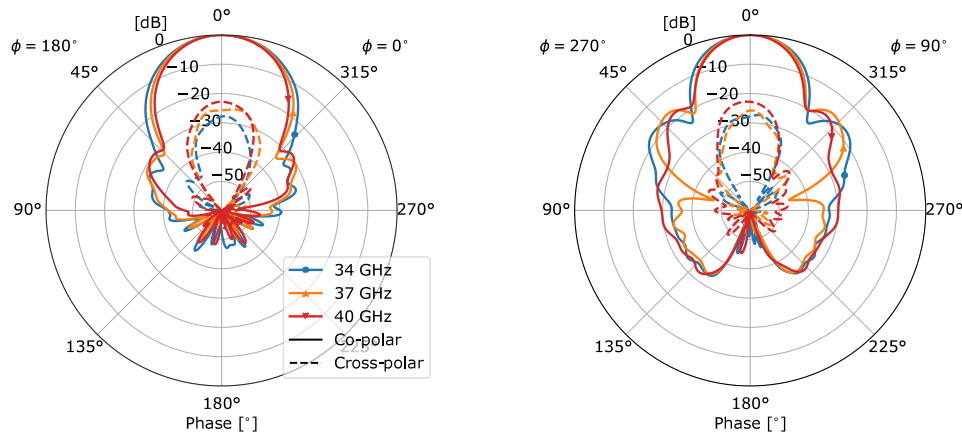

Fig. 11. Co- and cross-polar radiation patterns for the H-plane (left) and E-plane (right).
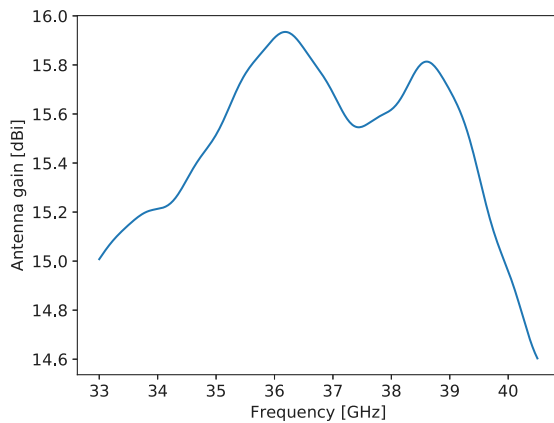

Fig. 12. Antenna gain along the boresight direction.

and G_R are, respectively, the transmitter and receiver antenna gains [dBi] that correspond to the antenna gains experimentally measured at the anechoic chamber (Fig. 12). L_T and L_R are the losses [dB] associated to transmitter and receiver adaptors and mismatching on the line (0.07 dB for given VSWR of 1.3), and L_{FS} the free space loss [dB]. As the calibration is done between the cable and the adaptor, the losses associated with the cables and DC blocks are considered in the measurements, and therefore do not need to be accounted for in the link budget. The free space losses can be estimated as

$$L_{FS} = 20 \log_{10} \left(\frac{4\pi d f}{c} \right),$$ (21)

where d is the distance between the antennas, f the operating frequency, and c the speed of light. For this experimental campaign the

antennas are positioned 2 m from each other outside of the chamber, next to the side windows of the Plasmatron.

Fig. 13 presents the magnitude of the measured S-parameters when the windows are opened (blue line) and closed (orange line), and the transmission coefficients, S_{12} and S_{21} parameters, are, additionally, overlapped with the theoretical link budget (grey line) as a function of the frequency. Regarding the transmitting coefficients, the ripples that differentiate the theoretical estimation and the magnitude measured without windows are due to the reflections on the walls. The additional ripples visible with windows are caused by the interference (constructive/destructive) of the multiple reflected waves on the windows. In average, there is an increase of 1.62 dB due to the reflection on the metallic walls and a decrease of 1.43 dB due to the presence of the quartz windows in the propagation path. Nevertheless, the attenuation due to the windows is dependent on the transmitting frequency, varying the difference with and without windows up to 22 dB. The increase in magnitude of the S_{11} and S_{22} parameters when introducing the windows indicates an increase of the reflected signal from each of the antennas. The lack of reciprocity between the S_{11} and S_{22} coefficients is caused by a slight misalignment of the antennas with respect to the respective window. This influences the way the waves reflect back on the windows but also on the walls of the chamber. To minimize the aforementioned effects, the influence of the plasma will be studied based on the difference between the signal with and without plasma (Eq. (15)).

6.3. Example of signal attenuation due to the plasma

Figs. 14(a) and 14(b) present the results for twenty and fifty samples of the S_{12} magnitude as a function of frequency (*sweep mode*) taken for an exemplifying test case at 15 mbar, and respectively without plasma and with plasma at 320 kW, 30 cm from the torch exit, each
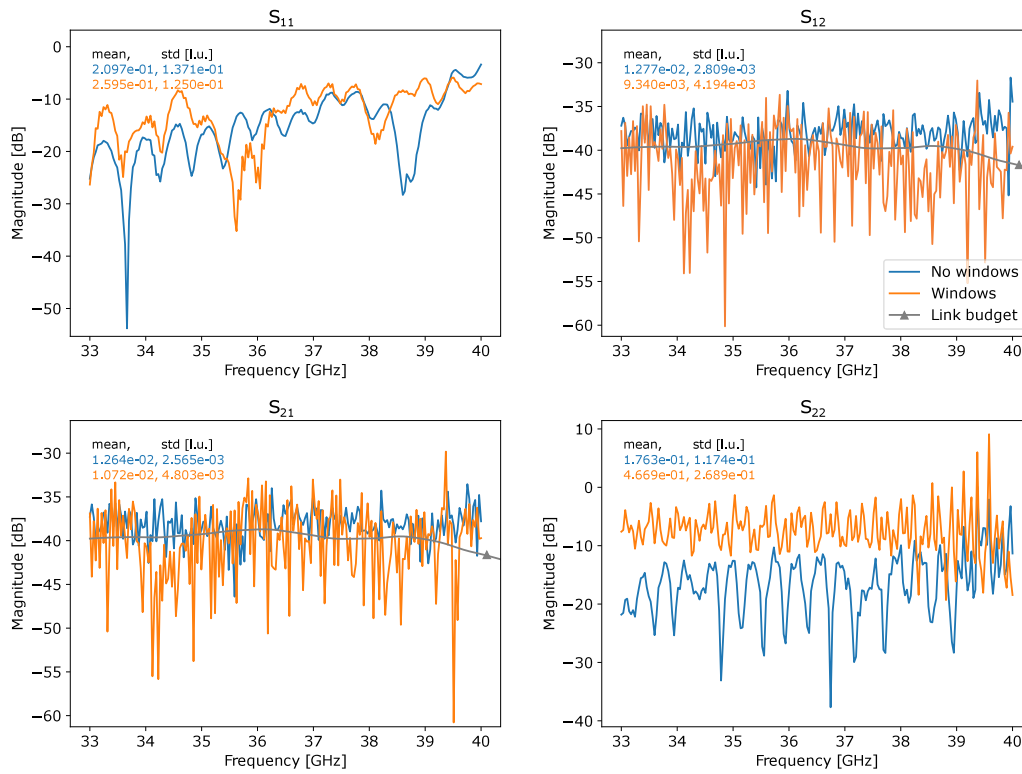
Fig. 13. Magnitude of the S-parameters with and without windows. (For interpretation of the references to colour in this figure legend, the reader is referred to the web version of this article.)
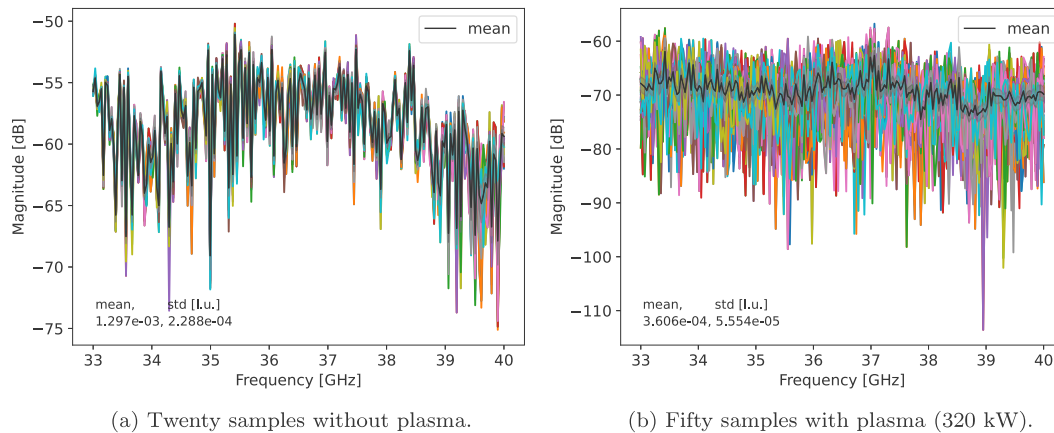

(a) Twenty samples without plasma.

(b) Fifty samples with plasma (320 kW).

Fig. 14. Magnitude of S_{12} parameter for 15 mbar, at 30 cm from the torch exit for the acquired samples.

overlapped with the mean and uncertainty bars (in black). The total mean and uncertainty, in linear units, are also presented. It is observed that without plasma the variations for each frequency are very small. The oscillations over the frequency range have also been observed and commented in Section 6.2, and are related with the ripples caused by the reflections on the walls. By comparing the different samples with plasma, it is visible that the local minima occurs at different frequencies depending on the timestamp of the recording, and therefore they are not repeatable. This phenomena is caused by the dynamic behaviour of the plasma jet, indicating that the thermodynamic state of the plasma changes during the frequency sweep performed by the VNA for each measurement [54]. Averaging the high amount of samples as a function of frequency to neglect the influence of the plasma unsteadiness and to consider a steady state flow. Simultaneously, the high number of samples taken for the case with plasma allows minimizing the uncertainty of the measurements.

For the same testing condition, Fig. 15 presents the mean magnitude of each of the S-parameters with a shadowed band corresponding to the uncertainty. The blue line corresponds to the signal without plasma and the orange line with plasma. Total averaged quantities and uncertainty values, in linear units, are also shown. It is observed that the mean magnitude of S_{11} and S_{22} for each frequency remains almost constant with the average values with and without plasma differing less than 1%. The high total standard deviation is due to the ripples visible throughout the measured frequency range. Conversely, the mean magnitude of the transmission coefficients over the tested frequency range decreases in average 11 dB when the signal propagates through the plasma. The instantaneous differences between S_{12} and S_{21} is assumed to be related to the operating principle of the VNA, that acquire each parameter sequentially. The delay between each acquisition may be enough for the state of the plasma to be changed between the acquisition of the two parameters.
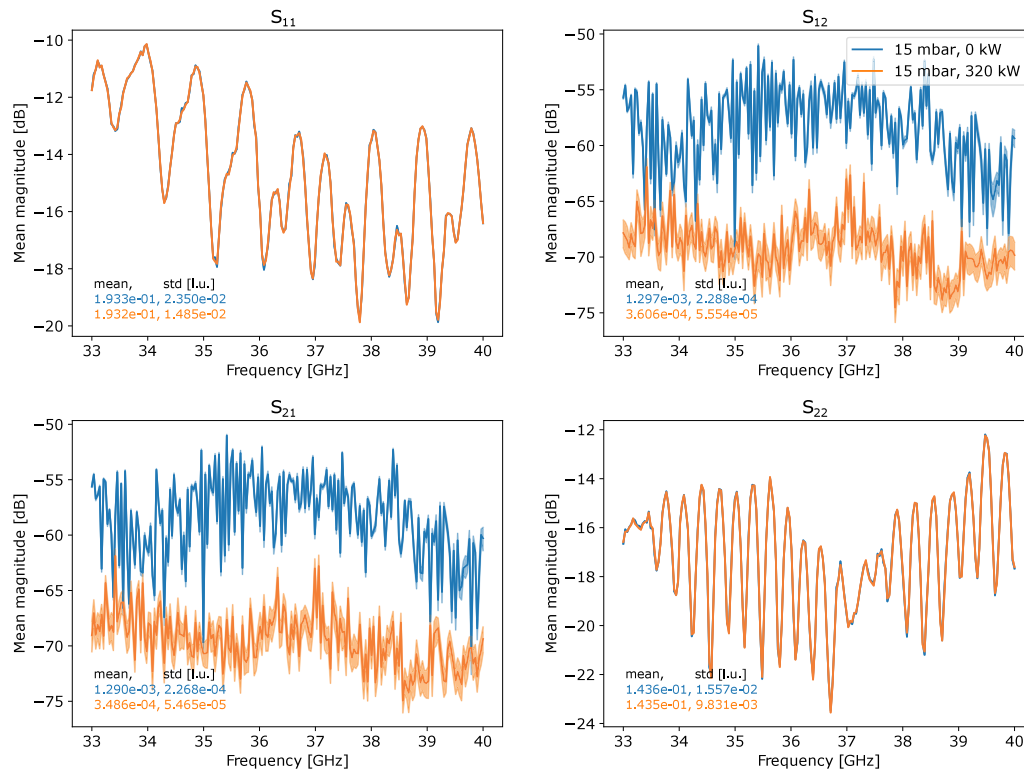
Fig. 15. Mean magnitude of the S-parameters for 15 mbar, 320 kW at 30 cm from the torch exit. (For interpretation of the references to colour in this figure legend, the reader is referred to the web version of this article.)

Hereafter, only the attenuation due to the plasma, i.e., the difference between with and without plasma (Eq. (16)) is considered, as exemplified for the same test case in Fig. 16. However it is important to note that, according to the ray tracing analysis presented in Section 5, new reflections occur due to the bending of the rays when propagating through an ionized medium. As such, some of the ripples observed in the attenuation evolution are caused by reflections on the wall that appear due to the deflections caused by the plasma, as seen in Fig. 8 for the corresponding numerical condition, which are not neglected by the background signal. This represents a limitation of the setup and on the analysis of the experimental results, but constitutes an inherent condition of the signal propagating through an ionized medium and which cannot be prevented in an experimental facility as the Plasmatron.

6.4. Steady state flow assumption: parametric study

Data analysis considering the dynamic nature of the plasma jet makes drawing conclusions about radio signal propagation in ionized medium challenging. Therefore, it is of interest to neglect the jet fluctuations, assume a steady state flow as normally done for thermal analysis in this type of facility [55], and consider total averaged quantities throughout the frequency range of each measurement. Thus, the mean attenuation for the S-parameters are plotted against power for different chamber pressure settings in Fig. 17. Uncertainties are also shown here as error bars around the mean value, following Eq. (19). The reflection coefficients are almost constant with power and different pressures. An exception is verified for the S_{11} parameter at 100 mbar, in which the ripples for the measurements with plasma are not occurring at the same frequencies as in the background signal. This is assumed to be due to a slight movement of the antenna between the acquisition of the background and plasma conditions, changing the interferences of the signal with the window, which are not neglected by the background. For the transmission coefficients, the signal drops that occur at certain frequencies due to the plasma instabilities increase the standard deviation of the signal magnitude.
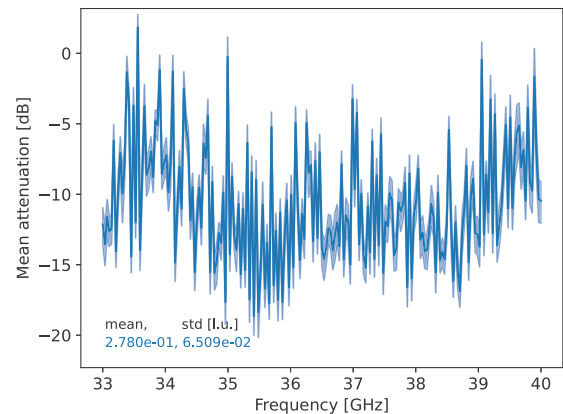

Fig. 16. Mean attenuation of the S_{12} parameter for 15 mbar, 320 kW at 30 cm from the torch exit.

To simplify the presentation and discussion of the results, the variation of the mean attenuation of the S_{12} transmission coefficient is plotted without error bars in Fig. 18, overlapped with the maximum electron number density (dotted lines). The electron number density distributions are obtained numerically with the COOLFluiD ICP solver and, for each condition, the maximum is extracted from the line of sight at 30 cm from the torch exit. For the transmission coefficients there is an increase of attenuation when increasing power, which tends to stabilizes from 320 kW. In fact, as seen from the 3D ray tracing results (Fig. 8) at around 320 kW, a very small amount of signal reaches the measurement area of the receiving antenna. This implies that when increasing power even further, almost no signal reaches directly the receiving antenna and the small signal magnitude received is due to reflections on the walls. Comparing the mean attenuation variation with power and the evolution of the maximum electron density they
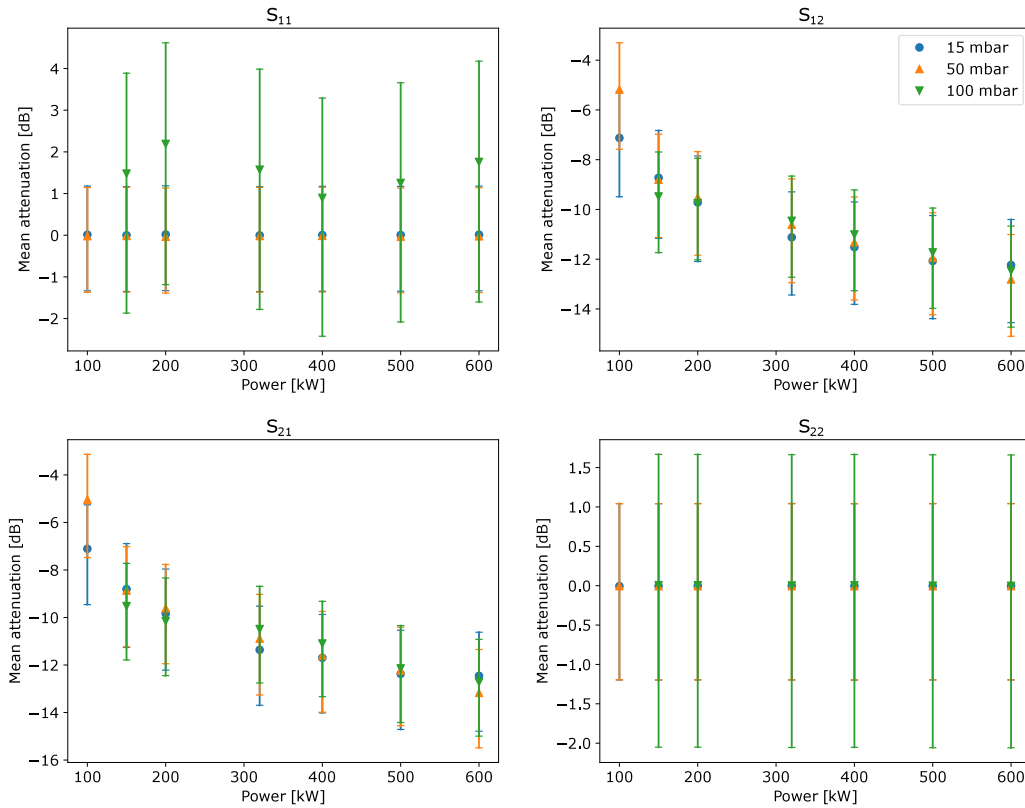
Fig. 17. Variation of the mean attenuation with error bars of the S-parameters at 30 cm from the torch exit.
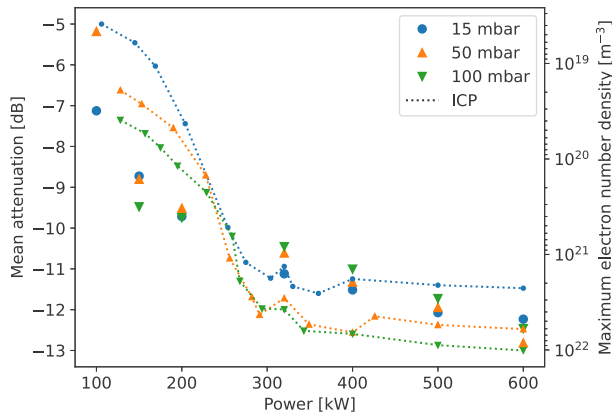

Fig. 18. Variation of the mean attenuation of the S_{12} parameter and maximum electron number density at 30 cm from the torch exit.
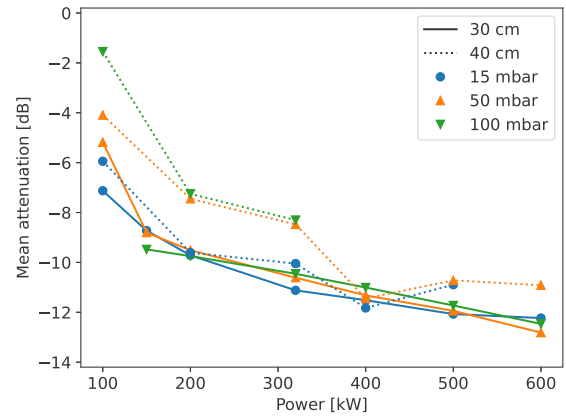

Fig. 19. Comparison between the S_{12} mean attenuation at 40 cm and 30 cm from the torch.

follow similar trends (right axis inverted), which is consistent with Eq. (5) as the attenuation increases with the increase of the electron densities. It is also seen that the mean attenuation of the transmission signal at 100 kW is higher from lower pressures, and it remains almost independent of pressure for the other powers. Interestingly, this fact contradicts the assumption of a plasma in LTE. Indeed, for mixtures in LTE the electron number density increases with pressure, and the signal attenuation is expected to follow the same behaviour. Therefore, experimental evidence indicates that the flow is not under LTE between 15 and 50 mbar. However, this statement should be verified by conducting experimental measurements of the electron number densities and comparing them with theoretical LTE assumptions. These measurements will be performed by computing the Stark broadening of the H_β line using optical emission spectroscopy.

6.4.1. Influence of the distance to the torch

Fig. 19 presents the variation of the mean attenuation as a function of power for a torch distance of 30 (full line) and 40 cm (dotted line). For the transmission coefficient, there is a clear increase of attenuation when increasing power for both of the positions of the antennas respect to the torch exit. For the same condition, the attenuation is higher for the antennas at 30 cm, as they are closer to the torch exit and the electron densities are higher (see Fig. 5). Overall the trends are the same when increasing power and pressure.

6.4.2. Polarization rotation

Another set of experiments conducted has one antenna (antenna 2) rotated 90° with respect to the other antenna. This way, a preliminary study about the polarization rotation due to the plasma can be done.
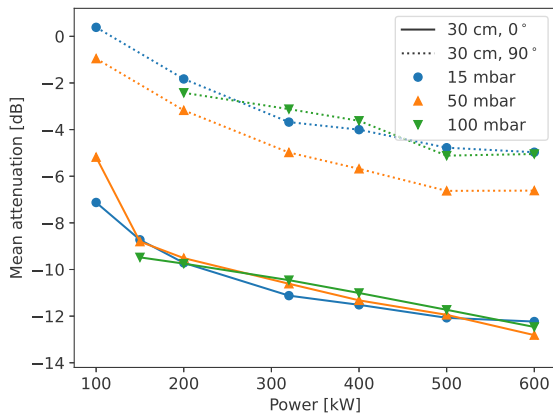
Fig. 20. Comparison between the S_{12} mean attenuation for an angle of 0° (label: *30 cm, 0°*) and 90° (label: *30 cm, 90°*) between the electric fields of each antenna at 30 cm from the torch exit.

In this configuration, the magnitude of the transmission coefficients, without plasma, intrinsically decreases around 10 dB due to the linear polarization of the antennas. Fig. 20 presents the variation of the S_{12} mean attenuation as a function of power and pressure when the electric field of both antennas is aligned (full line) and for when it is perpendicular (dotted line). In both cases the antennas are 30 cm from the torch exit. When turning on the plasma, the signal magnitude still decreases, indicating that there is still attenuation of the signal and consequently rotation of the its polarization. Comparing the transmission coefficient, the slope for the decrease in the mean attenuation for each of the coefficients is almost the same. At 15 mbar and 100 kW the difference is slightly higher than 0 dB when the electric fields are perpendicular. An attenuation higher than 0 dB means that the magnitude of signal received with the plasma is stronger than the magnitude of the signal without plasma. This positive magnitude difference indicates a Faraday rotation caused by the plasma and the Earth's magnetic field, but further investigation is required to validate these conclusions and to quantify the angle of rotation.

6.5. Measurements in different sampling modes

6.5.1. Single mode

Another way to neglect the dynamics of the plasma jet is to take measurements at a constant frequency using the VNA in *single mode*. During the VNA total acquisition time, multiple plasma oscillations occur. Thus, by measuring a large number of samples at the same

frequency through the total acquisition time (*single mode*), the mean magnitude is nearly constant and the standard deviation is small over the entire sweep time, neglecting the jet fluctuations.

Following this reasoning, Fig. 21(a) shows the variation of the mean attenuation of the S_{12} parameter with single central frequencies between 33 and 40 GHz (every 1 GHz) for 15, 50 and 100 mbar at 320 kW. In this case, the signal intensity is averaged over the 201 points in the central frequency and over the fifty samples acquired. For the transmission coefficient, there is a steep change on the mean attenuation at 35 GHz, while being fairly constant for the other frequencies. The same behaviour is observed for all the conditions tested, but not for the reflection coefficients. In fact, analysing Fig. 21(b) it is visible that the background mean magnitude for the S_{12} parameter drastically drops at 35 GHz, while the mean magnitude with plasma is not affected. Therefore, the mean attenuation decreases due to the background, which indicates that this phenomenon is intrinsic to the surrounding of the facility, and not related with the plasma itself.

6.5.2. Band mode

To analyse and eventually dump the punctual effect in the transmission coefficients at 35 GHz, a small frequency interval of ± 0.1 GHz is considered around the central frequency (*band mode*). As previously, the signal for each interval around the central frequency is averaged to obtain one point for that frequency. In this approach punctual sharp variations are dumped when averaging over the small interval measured. Fig. 22(a) presents the variation of the S_{12} coefficient mean attenuation with error bars for 15, 50 and 100 mbar and 320 kW as a function of frequency. With this configuration, the variation of the transmission coefficient is more regular when increasing frequency, and its behaviour is independent of the static pressure. The same trend as a function of frequency is observed for the other powers, as represented in Fig. 22(b) for the different powers tested at 15 mbar, and for the different static pressures. Moreover, from Fig. 22(b) a clear increase of the mean attenuation when increasing power is observed as also concluded from Fig. 17.

6.5.3. Acquisition modes comparison

The different methods can be compared by overlapping the results for the same operating condition. Fig. 23 shows this overlapping for a test case at 15 mbar, 320 kW as a function of frequency. Uncertainties for each of the measurements are also represented. The variation of the mean attenuation for the reflection coefficients (S_{11} and S_{22}) using the *single method* is assumed to be related to a slightly different alignment of the antennas in different test runs, as a new calibration and alignment are conducted at the beginning of each testing day. Nevertheless, the significant difference in the reflection coefficients is related with the drastic increase of the error bars when averaging the results over a
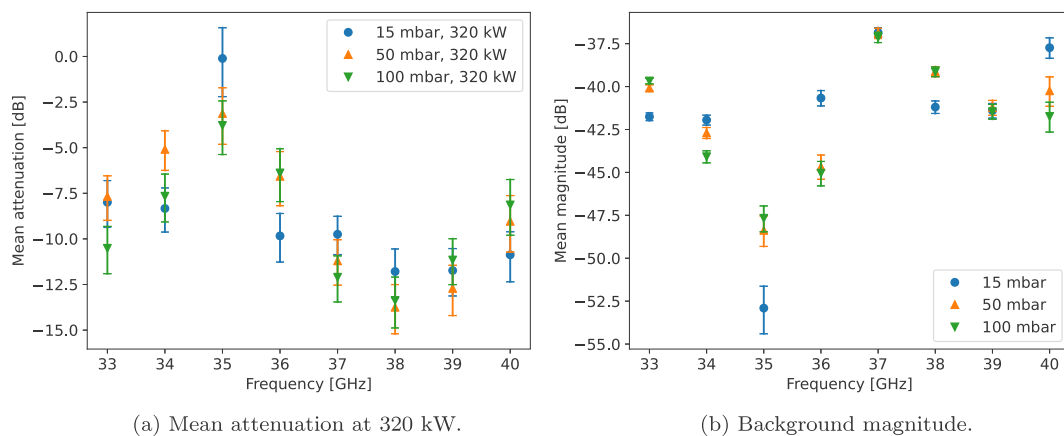

(a) Mean attenuation at 320 kW.

(b) Background magnitude.

Fig. 21. Variation of the mean attenuation and background magnitude of the S_{12} parameter as a function of each single frequency and power at 15, 50 and 100 mbar in *single mode*.
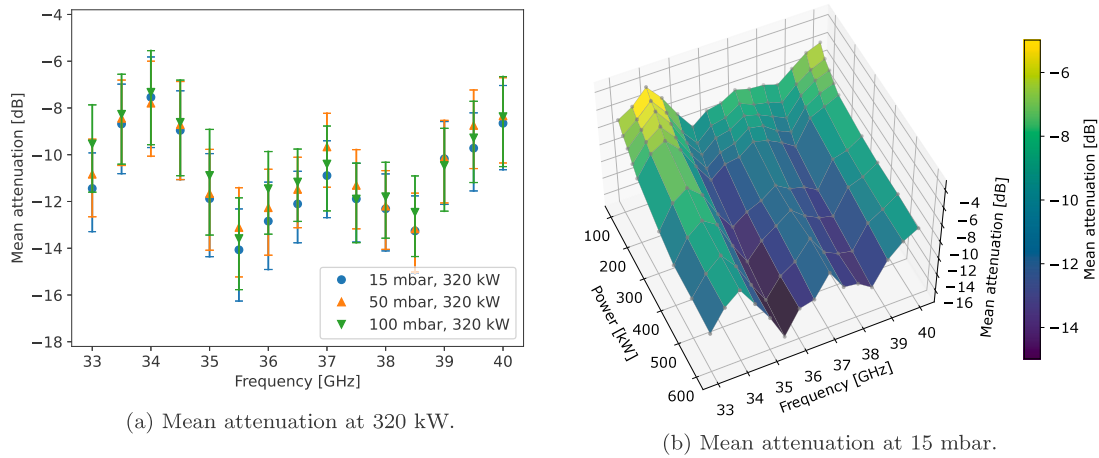
(a) Mean attenuation at 320 kW.

(b) Mean attenuation at 15 mbar.

Fig. 22. Variation of the mean attenuation of the S_{12} parameter as a function of pressure and frequency for 320 kW, and as a function of frequency and power at 15 mbar, in *band mode*.
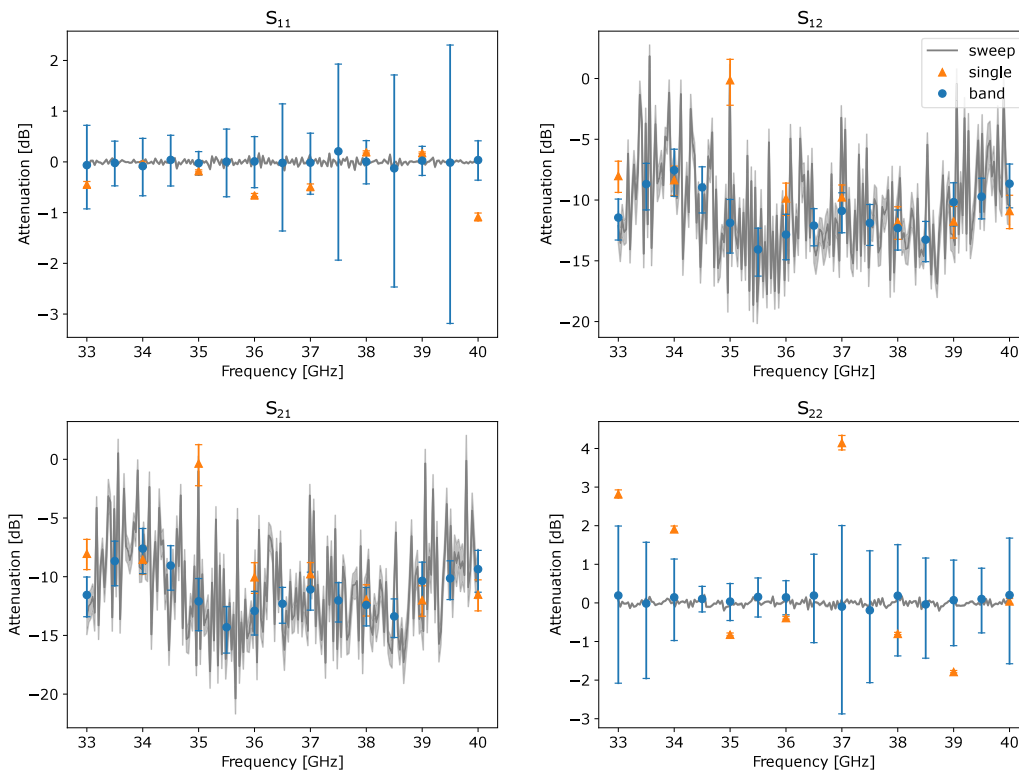

Fig. 23. Comparison of the variation of the mean attenuation of the S-parameters for each method (*sweep*, *single* and *band modes*) for 15 mbar, 320 kW.

small interval range around the central frequency (*band method*). By comparing the behaviour of the transmission coefficients, it is observed that the *sweep* and *band* methods give very similar results and trends. The *single* method overall also matches well the other two methods, except for 35 GHz, where there is a large variation of the mean attenuation, caused by the steep decrease of the background mean magnitude as presented previously in Fig. 21(b), which is not related with the plasma or the facility itself.

Ultimately, this comparison gives evidence and confidence on the repeatability of the experimental results. Overall, the *sweep mode* is considered the preferable method for acquiring the data since the error bars are smaller. Additionally, sweeping over frequency will allow to further estimate other signal effects caused by the plasma as time delay and dispersion.

7. Conclusions and future work

7.1. Conclusions

Radio signal propagation in an air plasma flow has been studied for a combination of static pressures and power settings, and acquisition modes. The design of the experimental setup for testing at the VKI-Plasmatron facility has been discussed, selecting the Ka-band as the most appropriate for blackout experiments. The signal propagation tests have been conducted by placing two conical horn antennas operating between 33 and 40 GHz across the plasma jet at the Plasmatron, and by measuring their signals with a vector network analyser. This approach constitutes a novelty for the study of the blackout phenomena. Ray tracing simulations have allowed to understand the numerical behaviour of the rays when propagating through a plasma flow, and

a full characterization of the antenna pattern, gain and half-power beamwidth has been performed at the UPC anechoic chamber.

The numerical analysis for the radio signal propagation has been conducted based on a combination of ICP simulations and the optical ray tracing method. The results have shown an interaction between the flow and the emitted signal, which consistently deflects more for higher electron number density on the jet. The characterization of the antenna has shown well-behaved broadside radiation patterns with low sidelobes and cross-polarization levels, and a quite constant gain along the boresight direction. The radio signal propagation has been studied initially without plasma to verify the effect of the windows and of the chamber walls, and evident ripples have been observed. A theoretical estimation of the ratio of the received and transmitted powers has allowed a comparison with the experimental results and a quantification of these effects.

To minimize these interferences, the attenuation due to the plasma has been studied based on the difference between the signal with and without plasma. As the state of the plasma is changing during one single VNA measurement, a direct comparison between each sample cannot be performed. Consequently, to neglect the influence of the plasma unsteadiness, the signal has been averaged over the frequency sweep range. Clear attenuations of the signal have been verified, ranging between 2 and 15 dB depending on the testing conditions. The evolution of the variation of the mean attenuation as a function of power has been found to follow the same trend of the numerical electron number densities, as expected. This represents a preliminary comparison with electron number density, since this quantity is not precisely known. For the lowest power, a higher attenuation has been verified for the lowest pressure, contradicting the assumption of LTE. No significant changes with pressure have been verified for higher powers. The parametric study conducted by moving the antennas further from the torch exit has shown a lower attenuation, due to the lower density of electrons further from the torch exit. Preliminary evidence of Faraday rotation has also been observed. A comparison between the different acquisition modes has shown that overall the results are comparable, indicating that the measurements are repeatable.

7.2. Future work

Based on the experimental results presented, the following future work is recommended:

1. testing with more directive antennas to reduce the amount of reflections on the chamber walls;
2. quantification of the Faraday rotation due to the plasma flow and magnetic field of the Earth;
3. measurement of the temperature and electron number densities in the Plasmatron facility using emission spectroscopy, for correlation with the electric power, and comparison with the signal attenuation measurements and with the ICP numerical estimations used for the ray tracing simulations;
4. verification of the LTE assumption at low pressures;
5. measurement of the signal propagating through a stagnant flow (instead of side to side window).

Declaration of competing interest

The authors declare the following financial interests/personal relationships which may be considered as potential competing interests: Diana Luis reports financial support was provided by Foundation for Science and Technology. Vincent Giangaspero reports financial support was provided by Research Foundation Flanders. Diana Luis, Vincent Giangaspero, Alan Viladegut, Andrea Lani, and Olivier Chazot report financial support and article publishing charges were provided by EU Framework Programme for Research and Innovation Future and Emerging Technologies.

References

[1] M. Keidar, M. Kim, I. Boyd, Electromagnetic reduction of plasma density during atmospheric reentry and hypersonic flights, J. Spacecr. Rockets 45 (3) (2008) http://dx.doi.org/10.2514/1.32147, 445–453.

[2] P. Tran, J.C. Paulat, P. Boukhobza, Re-entry flight experiments lessons learned – The atmospheric reentry demonstrator ARD, in: Flight Experiments for Hypersonic Vehicle Development, 2007, 10–1–10–46, Education Notes RTO-EN-AVT-130.

[3] J.W. Marini, F.W. Hager, Apollo 6, 7 and 8 Blackout Test Results, Technical Report NASA TM X-63636, Goddard Space Flight Center, 1969.

[4] W.L. Grantham, Flight Results of a 25 000-Foot-Persecond Reentry Experiment Using Microwave Reflectometers to Measure Plasma Electron Density and Stand-off Distances, NASA Technical Note D-6062, NASA Langley Research Center, 1970.

[5] W.L. Jones, A.E. Cross, Electrostatic-Probe Measurements of Plasma Parameters for Two Reentry Flight Experiments at 25000 Feet per Second, Technical Note NASA TN D-6617, NASA Langley Research Center, 1972.

[6] R.P. Starkey, Hypersonic vehicle telemetry blackout analysis, J. Spacecr. Rockets 52 (2) (2015) http://dx.doi.org/10.2514/1.A32051.

[7] R.P. Starkey, M.J. Lewis, C.H. Jones, Active flowfield modification for plasma telemetry, in: International Test and Evaluation Association Conference ITEA, 2002.

[8] S.V. Nazarenko, A.C. Newll, V.E. Zakharov, Communication through plasma sheaths via Raman (three-wave) scattering process, Phys. Plasmas 1 (9) (1994) 2827–2834, http://dx.doi.org/10.1063/1.870521.

[9] R.A. Hartunian, G.E. Stewart, S.D. Fergason, T.J. Curtiss, R.W. Seibold, Causes and Mitigation of Radio Frequency (RF) Blackout During Reentry of Reusable Launch Vehicles, Technical Report ART-2007(5309)-1, The Aerospace Corporation, 2007.

[10] W.A. Imbriale, S. Gao, L. Boccia (Eds.), Space Antenna Handbook, John Wiley & Sons, Inc, ISBN: 978-1-119-99319-3, 2012.

[11] H. Zhou, X. Li, K. Xie, Y. Liu, Y. Yu, Mitigating reentry radio blackout by using a traveling magnetic field, AIP Adv. 7 (105314) (2017) http://dx.doi.org/10.1063/1.4999039.

[12] M. Kim, Electromagnetic Manipulation of Plasma Layer for Re-Entry Blackout Mitigation (Ph.D. thesis), Department of Aerospace Engineering, University of Michigan, 2009.

[13] J.P. Rybak, R.J. Churchill, Progress in reentry communications, IEEE Trans. Aerosp. Electron. Syst. AES-7 (5) (1971) 879–894, http://dx.doi.org/10.1109/TAES.1971.310328.

[14] C. Jones, Report from the Workshop on Communications Through Plasma During Hypersonic Flight, AIAA Meeting Paper, 2006, p. 25, http://dx.doi.org/10.2514/6.2009-1718.

[15] E. Gillman, J. Foster, I. Blankson, Review of Leading Approaches for Mitigating Hypersonic Vehicle Communications Blackout and a Method of Ceramic Particulate Injection Via Cathode Spot Arcs for Blackout Mitigation, Technical Report NASA/TM - 2010-216220, NASA, 2010.

[16] I.F. Belov, V.Y. Borovoy, V.A. Gorelov, A.Y. Kireev, A.S. Korolev, E.A. Stepanov, Investigation of remote antenna assembly for radio communication with reentry vehicle, J. Spacecr. Rockets 38 (2) (2001) 249–256, http://dx.doi.org/10.2514/2.3678.

[17] R. Savino, D. Paterna, M. De Stefano Fumo, M. D'Eli, Plasma-radiofrequency interactions around atmospheric re-entry vehicles: Modelling and arc-jet simulation, Open Aerosp. Eng. J. 3 (2010) 76–85, http://dx.doi.org/10.2174/1874146001003010076.

[18] S.A. Bendoukha, K. Okuyama, B. Szasz, S. Takayuki, Experimental method using arc wind tunnel to simulate a new technique for communicating with a reentry probe having a thermal shield made of LATS materials, Int. J. Res. 5 (2017) 1–12, http://dx.doi.org/10.5281/zenodo.345434.

[19] V.F. Giangaspero, V. Sharma, J. Laur, J. Thoemel, A. Munafò, A. Lani, S. Poedts, 3D ray tracing solver for communication blackout analysis in atmospheric entry missions, Comput. Phys. Comm. 286 (108663) (2023) http://dx.doi.org/10.1016/j.cpc.2023.108663.

[20] D. Morabito, R. Kornfeld, K. Bruvold, L. Craig, K. Edquist, The Mars phoenix communications brownout during entry into the Martian atmosphere, in: The Interplanetary Network Progress Report 42-179, 2009.

[21] D.D. Morabito, B. Schratz, K. Bruvold, P. Ilott, K. Edquist, A.D. Cianciolo, The Mars science laboratory EDL communications brownout and blackout at UHF, in: The Interplanetary Network Progress Report 42-197, 2014.

[22] S. Ramjatan, T. Magin, T. Scholz, V. Van der Hagen, J. Thoemel, Blackout analysis of small cone-shaped reentry vehicles, J. Thermophys. Heat Transfer 31 (2) (2016) 269–282, http://dx.doi.org/10.2514/1.T4825.

[23] C. Vecchi, M. Sabbadini, R. Maggiora, A. Siciliano, Modelling of antenna radiation pattern of a re-entry vehicle in presence of plasma, in: IEEE Antennas and Propagation Society Symposium, 2004, http://dx.doi.org/10.1109/APS.2004.1329583.

[24] Y. Takahashi, R. Nakasato, N. Oshima, Analysis of radio frequency blackout for a blunt-body capsule in atmospheric reentry missions, Aerospace 3 (1) (2016) http://dx.doi.org/10.3390/aerospace3010002.

[25] S. Ramjatan, A. Lani, S. Boccelli, B. Van Hove, Ö. Karatekin, T. Magin, J. Thoemel, Blackout analysis of Mars entry missions, J. Fluid Mech. 904 (A26) (2020) http://dx.doi.org/10.1017/jfm.2020.714.

[26] V.F. Giangaspero, T. Magin, A. Lani, S. Poedts, Modeling strategy for blackout analysis of re-entry phases in space exploration missions, in: T. Magin (Ed.), Review of the VKI Doctoral Research 2021-2022, von Karman Institute for Fluid Dynamics, ISBN: 978-2-87516-187-1, 2022.

[27] V.F. Giangaspero, V. Sharma, J. Laur, J. Thoemel, S. Poedts, A. Lani, Ray tracing analysis of high frequency communication system in inductively coupled plasma facility, in: 9th European Conference for Aeronautics and Space Sciences, EUCASS, 2022, http://dx.doi.org/10.13009/EUCASS2022-6181.

[28] J.S. Laur, V.F. Giangaspero, V. Sharma, A. Lani, N. Donaldson, M.K. Kim, J. Giacomelli, G. Herdrich, A. Hein, J. Thoemel, The effect of an applied magnetic field onto re-entry radio communication blackout, in: 2nd International Conference on Flight Vehicles, Aerothermodynamics and Re-Entry Missions Engineering, FAR, 2022.

[29] V. Sharma, J. Giacomelli, N. Donaldson, V.F. Giangaspero, A. Lani, G. Herdrich, M. Kim, A. Munafo, S. Poedts, Assessment of CFD capabilities of various in-house solvers for modeling argon plasma MHD experiments, in: 9th International Workshop on Radiation of High Temperature Gases for Space Missions (RHTG-9), 2022.

[30] A. Lani, V. Sharma, V.F. Giangaspero, et al., A Magnetohydrodynamic enhanced entry system for space transportation: MEESST, J. Space Saf. Eng. 10 (1) (2023) http://dx.doi.org/10.1016/j.jsse.2022.11.004.

[31] M.R. Betancourt, M. Collier-Wright, E. Bögel, et al., Magnetohydrodynamic Enhanced Entry System for Space Transportation (MEESST) as a key building block for low-cost interplanetary missions, J. Br. Interplanet. Soc. (2021) http://dx.doi.org/10.5445/IR/1000141932.

[32] R. Starkey, R. Lewis, C. Jones, Plasma telemetry in hypersonic flight, in: International Telemetering Conference, International Foundation for Telemetering, 2002, Paper 02-15-2.

[33] R. Starkey, R. Lewis, C. Jones, Electromagnetic wave / magnetoactive plasma sheath interaction for hypersonic vehicle telemetry blackout analysis, in: 34th AIAA Plasmadynamics and Lasers Conference, AIAA Paper 2003-4167, 2003, http://dx.doi.org/10.2514/6.2003-4167.

[34] M. Kim, Active plasma layer manipulation scheme during hypersonic flight, Aerosp. Sci. Technol. 35 (2014) 135–142, http://dx.doi.org/10.1016/j.ast.2014.03.008.

[35] M. Kim, A. Gülhan, Plasma manipulation using a MHD-based device for a communication blackout in hypersonic flights, in: Proceedings of 5th International Conference on Recent Advances in Space Technologies, Vol. RAST2011, 2011, pp. 412–417, http://dx.doi.org/10.1109/RAST.2011.5966868.

[36] K. Davies, Ionospheric Radio Propagation, Vol. 80, US Department of Commerce, National Bureau of Standards, 1965.

[37] F. Caspers, RF engineering basic concepts: S-parameters, in: CERN Yellow Report, CERN-2011-007, 2011, pp. 67–93, http://dx.doi.org/10.48550/arXiv.1201.2346.

[38] C.A. Balanis, Antenna Theory: Analysis and Design, second ed., John Wiley & Sons, Inc, ISBN: 0-471-59268-4, 1938.

[39] G. Miller, Radiation Patterns and Antenna Characteristics, Technical report, Keysight Knowledge Center, 2008, https://edadocs.software.keysight.com/display/ads2008U2/Radiation+Patterns+and+Antenna+Characteristics, last accessed 14 November 2022.

[40] B. Bottin, O. Chazot, M. Carbonaro, V. Van Der Haegen, S. Paris, The VKI plasmatron characteristics and performance, in: Measurement Techniques for High Enthalpy and Plasma Flows, 2000.

[41] B. Bottin, Aerothermodynamic Model of an Inductively-Coupled Plasma Wind Tunnel: Numerical and Experimental Determination of the Facility Performance (Ph.D. thesis), von Karman Institue for Fluid Dynamics, 1999.

[42] A. Viladegut, Assessment of Gas-Surface Interaction Modelling for Lifting Body Re-Entry Flight Design (Ph.D. thesis), von Karman Institute for Fluid Dynamics and Universitàt Politècnica de Catalunya, 2017.

[43] A. Fagnani, D. Le Quang Huy, B. Helber, S. Demange, A. Turchi, O. Chazot, A. Hubin, Investigation of a free-stream air plasma flow by optical emission spectroscopy and comparison to magnetohydrodynamics simulations, in: AIAA SciTech Forum, 2020.

[44] F. Panerai, Aerothermochemistry Characterization of Thermal Protection Systems (Ph.D. thesis), von Karman Institute for Fluid Dynamics and Università degli Studi di Perugia, 2012.

[45] Anechoic Chamber, Universitat Politècnica de Catalunya, https://www.tsc.upc.edu/en/facilities/anechoic-chamber, last accessed 15 March 2023.

[46] S. Beraza, V. González-Gambau, F. Torres, N. Ubeda, I. Corbella, S. Blanch, A. Camps, M. Vall-llossera, J.L. Alvarez-Perez, S. Ribo, M. Martin-Neira, MIRAS-SMOS demonstrator test campaigns at Polytechnic University of Catalonia, in: IEEE International Geoscience & Remote Sensing Symposium, IGARSS 2006, 2006, http://dx.doi.org/10.1109/IGARSS.2006.459.

[47] J. Appel-Hansen, Near-field far-field antenna measurements, in: Y.T. Lo, S.W. Lee (Eds.), Antenna Handbook, Springer, 1988, pp. 2175–2205, http://dx.doi.org/10.1007/978-1-4615-6459-1_33, chapter 33.

[48] G. Degrez, D. Vanden Abeele, P. Barbante, B. Bottin, Numerical simulation of inductively coupled plasma flows under chemical non-equilibrium, Internat. J. Numer. Methods Heat Fluid Flow 14 (4) (2004) 538–558, http://dx.doi.org/10.1108/09615530410532286.

[49] D. Vanden Abeele, G. Degrez, Efficient computational model for inductive plasmas flows, AIAA J. 38 (2) (2000) 234–242, http://dx.doi.org/10.2514/2.977.

[50] A. Lani, An Object Oriented and High Performance Platform for Aerothermodynamics Simulation (Ph.D. thesis), Université Libre de Bruxelles and von Karman Institute for Fluid Dynamics, 2008.

[51] M.J.B. Scoggins, Development of Numerical Methods and Study of Coupled Flow, Radiation, and Ablation Phenomena for Atmospheric Entry (Ph.D. thesis), von Karman Institute for Fluid Dynamics and CentraleSupélec, 2017.

[52] H. Ling, R.-C. Chou, S.-W. Lee, Shooting and bouncing rays: calculating the RCS of an arbitrarily shaped cavity, IEEE Trans. Antennas and Propagation 37 (2) (1989) 194–205, http://dx.doi.org/10.1109/8.18706.

[53] Y.A. Kravtsov, Y.I. Orlov, Geometrical Optics of Inhomogeneous Media, in: Springer Series on Wave Phenomena, vol. 38, Springer, Berlin, Heidelberg, ISBN: 978-3-642-84033-3, 1990.

[54] D. Luís, A. Viladegut, A. Camps, O. Chazot, Effect of electron number densities on the radio signal attenuation in an inductively coupled plasma facility, in: 9th European Conference for Aeronautics and Space Sciences, EUCASS, 2022, http://dx.doi.org/10.13009/EUCASS2022-6128.

[55] A. Cipullo, B. Helber, F. Panerai, L. Zeni, O. Chazot, Investigation of freestream plasma flow produced by inductively coupled plasma wind tunnel, J. Thermophys. Heat Transfer 28 (3) (2014).